applied sciences

MDPI

Article

Multiphysics Analysis of Transient Muzzle Arc Evolution and Arc-Induced Dynamic Disturbance in Electromagnetic Rail Launch

Jianyong Lou [1,*], Jianghan Yan [1], Xiyuan Tian [1], Chao Chen [1], Qian Liu [1] and Yigong Feng [2]

[1] School of Electrical Engineering, Xi'an Jiaotong University, Xi'an 710049, China; jhyan@stu.xjtu.edu.cn (J.Y.); tianxiyuan02@163.com (X.T.); 15070548553@163.com (C.C.); lauhim@stu.xjtu.edu.cn (Q.L.)
[2] State Grid Henan Electric Power Company Construction Branch, Zhengzhou 450052, China; fengyigong0313@stu.xjtu.edu.cn
* Correspondence: jylou@mail.xjtu.edu.cn

Abstract

To investigate the transient muzzle arc and its influence on the post-exit dynamics of the armature in electromagnetic rail launch (EMRL) systems, a bidirectionally coupled multiphysics simulation framework integrating ANSYS Maxwell and Fluent is developed. A 10 × 10 mm scaled-caliber launcher with a 1.9 g aluminum-alloy armature is considered to quantitatively characterize the coupled evolution of the electromagnetic field, temperature field, and arc-induced flow field after armature–rail separation. The results show that the air-gap breakdown arc reaches a peak temperature of approximately 35,873 K at the early post-exit stage, producing concentrated thermal loads near the armature tail and rail leading edges. The rapid spatial expansion of the arc further redistributes the current density and distorts the local electromagnetic field, resulting in asymmetric Lorentz forces acting on the unconstrained armature and pronounced transient acceleration disturbances along multiple axes. Comparative simulations with and without a bypass arc chute demonstrate that the additional conduction path promotes rapid current commutation and suppresses the spatial expansion and persistence of the muzzle arc. Consequently, the arc-induced electromagnetic disturbance is substantially reduced, and the armature acceleration responses converge toward zero within approximately 50 μs after muzzle exit. These results establish a quantitative link between transient arc evolution, electromagnetic-field distortion, and post-exit armature dynamic disturbance, and demonstrate the potential of bypass arc chutes for simultaneously mitigating muzzle thermal loading and improving post-exit flight stability in EMRL systems.

Keywords: electromagnetic rail launch; muzzle transient arc; Lorentz force; transient overload; arc chute; multi-physics bidirectional coupling

Check for updates

Academic Editor: Paolo Renna

Received: 27 August 2026
Revised: 17 September 2026
Accepted: 18 September 2026
Published: 20 September 2026

Copyright: © 2026 by the authors. Licensee MDPI, Basel, Switzerland. This article is an open access article distributed under the terms and conditions of the Creative Commons Attribution (CC BY) license.

1. Introduction

Electromagnetic rail launch (EMRL) technology has attracted increasing attention in military defense, aerospace propulsion, and high-speed impact applications because of its high launch velocity, high kinetic energy output, and controllable acceleration characteristics [1–3]. During the launch process, a high-current pulse flows through the conductive loop formed by the rails and armature, generating a strong magnetic field and producing a Lorentz force that accelerates the armature along the launch direction [4,5]. However, when the armature approaches the muzzle and separates from the rails, the continuous

electrical contact is abruptly interrupted, resulting in the formation of a transient air gap in the current path [6]. Owing to the inductive energy stored in the launch circuit, the residual current cannot decay instantaneously, producing a rapid voltage rise across the gap. When the local electric field exceeds the breakdown threshold, dielectric breakdown occurs, resulting in the formation of a high-temperature transient muzzle arc plasma [7–9].

The transient muzzle arc poses significant challenges to both the structural integrity and dynamic performance of EMRL systems. From the thermal perspective, the extremely high plasma temperature produces concentrated thermal loading near the rail exit region and armature tail, resulting in strong thermal exposure and potential thermally induced material damage [10,11]. Such thermal damage can progressively reduce rail service life and increase the risk of structural degradation in the muzzle region. From the electromagnetic perspective, the rapid expansion and deformation of the arc plasma redistribute the local current density and modify the electromagnetic field topology, producing an asymmetric electromagnetic environment near the muzzle [12]. Once the armature loses the mechanical constraint provided by the rails, the resulting nonuniform Lorentz force acts directly on the armature and may generate transient acceleration disturbances along multiple directions. For lightweight armatures, these asymmetric electromagnetic loads can cause significant deviations in the post-exit motion state and adversely affect the stability of the transitional free-flight stage, thereby potentially degrading launch accuracy [13]. Therefore, understanding the coupled evolution of the transient muzzle arc and its induced electromagnetic and dynamic disturbances is essential for improving the reliability and operational performance of EMRL systems.

To mitigate the destructive effects of muzzle arcs, various arc-suppression approaches based on current-path regulation and residual electromagnetic energy dissipation have been investigated [14]. Previous studies have mainly focused on arc formation characteristics, rail erosion, contact behavior, and thermal damage through experimental measurements and numerical simulations [15,16]. Despite these efforts, several important issues remain unresolved. First, existing numerical investigations have predominantly concentrated on the electromagnetic launch process within the rails, whereas the transient arc evolution immediately after armature–rail separation has received comparatively less attention. Second, many multiphysics models adopt simplified or one-way coupling strategies, in which electromagnetic, thermal, or plasma-related processes are treated separately, thereby limiting the ability to capture the dynamic feedback between temperature-dependent conductivity, plasma evolution, and electromagnetic-field redistribution [17,18]. More importantly, the quantitative relationship between spatially asymmetric arc evolution, electromagnetic-force redistribution, and post-exit armature dynamics has rarely been investigated from a unified transient perspective. Existing arc-suppression studies have also primarily emphasized thermal protection and residual-energy dissipation, while the effectiveness of suppression structures in reducing electromagnetic disturbances and stabilizing the post-exit armature motion remains insufficiently clarified.

To address these limitations, this paper develops a high-fidelity transient bidirectional multiphysics coupling framework based on the Ansys System Coupling platform (2025R2). A coupled Maxwell–Fluent model is established to capture the transient interaction among the electromagnetic field, temperature field, and plasma flow field during muzzle arc evolution. A 10 mm $\times$ 10 mm scaled-caliber electromagnetic launcher equipped with a 1.9 g aluminum-alloy U-shaped armature is considered as the research object. The model incorporates the mutual interaction among electromagnetic excitation, Joule heating, temperature-dependent electrical conductivity, and plasma evolution, enabling the transient reconstruction of the coupled arc evolution following armature–rail separation. Furthermore, comparative simulations are performed for the “Without Arc Chute” and

"With Arc Chute" configurations to investigate the suppression mechanism of the bypass arc device [19]. The effects of the arc-suppression structure on the transient thermal field, electromagnetic-force distribution, and post-exit armature acceleration are quantitatively evaluated. The results establish a direct physical connection between transient muzzle arc evolution, electromagnetic-field distortion, and armature dynamic disturbance, while demonstrating the potential of bypass arc chutes for simultaneously mitigating thermal loading and improving post-exit dynamic stability [20].

The main contributions of this study are summarized as follows:

A transient bidirectional multiphysics coupling framework is developed to characterize the coupled evolution of the electromagnetic, thermal, and plasma flow fields during the post-exit muzzle-arc process.

The relationship between muzzle-arc evolution and armature dynamic disturbance is quantitatively clarified, linking arc expansion and current-density redistribution to electromagnetic-field distortion, asymmetric Lorentz forces, and transient multidirectional acceleration.

The effectiveness of a bypass arc chute is quantitatively evaluated by comparing the thermal, electromagnetic, and armature dynamic responses with and without the suppression structure.

2. Multiphysics Numerical Model

2.1. Geometry of Electromagnetic Rail Launcher

To investigate the transient evolution of the muzzle arc following armature–rail separation and its effects on the electromagnetic loading and translational dynamic response of the armature, a three-dimensional geometric model comprising the rails, a U-shaped armature, and a bypass arc chute is established, as illustrated in Figure 1. The numerical model represents a scaled electromagnetic launcher with a muzzle caliber of 10 mm × 10 mm. The armature is modeled as a 1.9 g aluminum-alloy U-shaped structure with translational motion along the launch direction, while rotational degrees of freedom are not considered in the present study. Two pairs of steel bypass arc chutes are symmetrically arranged outside the muzzle region. The overall dimensions of each arc-chute body are 9 mm × 9 mm × 9 mm, the arc-initiating section has a cross-sectional size of 5 mm × 8 mm, and the gap between the arc-chute components is 2 mm. The bypass arc chute is configured to provide a low-impedance branch for current redistribution after arc initiation. The corresponding material properties of the armature, rails, and arc chute are listed in Table 1. The net electromagnetic force acting on the armature is obtained by volume integration of the local Lorentz-force density calculated by ANSYS Maxwell and is subsequently used to evaluate the translational acceleration response.

Table 1. Units for magnetic properties.

Module	Electrical Conductivity	Thermal Conductivity	Specific Heat Capacity/ J/(kg·K)
Armature (Aluminum Alloy)	2.1×10^7 S/m	130 W/(m·K)	875 J/(kg·K)
Rails (Copper)	5.8×10^7 S/m	385 W/(m·K)	385 J/(kg·K)
Arc Chutes (Steel)	2.0×10^6 S/m	45 W/(m·K)	480 J/(kg·K)

The armature adopts a 1.9 g U-shaped structure, with Aluminum selected as its material in ANSYS Fluent. Two pairs of Steel bypass arc chutes are symmetrically arranged outside the muzzle, while the rails are modeled using Copper. The corresponding solid-region material properties used in the numerical model are listed in Table 1.

During the electromagnetic launch process, the upper and lower rails serve as the positive and negative terminals of the main current circuit, respectively, providing the electromagnetic driving path for the armature. A constant current of 18 kA is prescribed at the rail terminals throughout the simulated time interval, as shown in Figure 2. This controlled excitation is adopted to investigate the transient evolution of the muzzle arc and its associated electromagnetic, thermal, and dynamic responses after armature–rail separation.

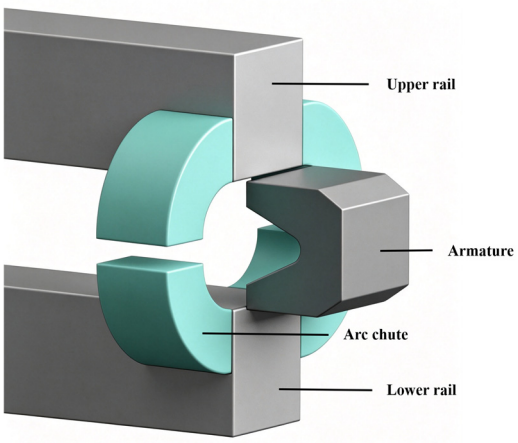


Figure 1. Three-dimensional geometry of the rail launcher with the arc chute.

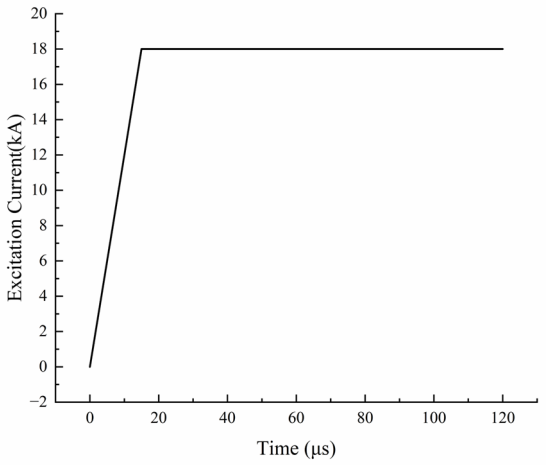


Figure 2. Prescribed 18 kA constant-current excitation applied at the rail terminals.

As the armature moves toward the muzzle and gradually separates from the rails, the conductive path is interrupted, forming a transient air gap between the rail exit and the armature tail. After armature–rail separation, the interruption of the original conductive path produces a rapidly increasing gap impedance and promotes the formation of a plasma conduction channel under the prescribed current excitation.

To reduce the arc energy of the main circuit, a bypass arc chute is arranged outside the muzzle exit. After arc initiation, this structure provides a low-impedance shunt path, forcing the residual current to commutate from the main circuit to the bypass branch. Accordingly, the arc intensity is suppressed, and thermal loading and asymmetric electromagnetic loading are alleviated. Since the muzzle arc is highly concentrated near the exit region, the computational domain mainly covers the leading edges of the rails, the armature tail, and the air domain surrounding the arc chute to balance computational accuracy and computational cost.

2.2. Model Assumptions

The transient muzzle arc involves strongly coupled electromagnetic, thermal, and fluid processes over a wide range of plasma states. To establish a computationally tractable macroscopic model, the following physical assumptions and numerical treatments are adopted.

Single-Fluid Magnetohydrodynamics (MHD) Assumption: The arc plasma is treated as a single, continuous, and quasi-neutral conducting fluid. The relative drift between electrons and heavy particles is not explicitly resolved, and the plasma dynamics are described using the macroscopic conservation equations of mass, momentum, and energy.

Local Thermodynamic Equilibrium (LTE) Assumption: The arc plasma is modeled under the local thermodynamic equilibrium (LTE) assumption, under which the electron and heavy-particle temperatures are represented by a common thermodynamic temperature T. This approximation is primarily applied to the established, high-temperature bulk plasma region, where frequent particle collisions promote thermal coupling and where LTE-based macroscopic MHD models are commonly used for describing the arc-column dynamics. However, deviations from LTE can occur during the initial arc formation, in low-temperature peripheral regions, and in the near-electrode sheath regions because of strong gradients, high electric fields, and insufficient collisional energy exchange. The present model does not explicitly resolve electron–heavy-particle thermal nonequilibrium or sheath-scale physics. Therefore, the LTE assumption is adopted to describe the macroscopic evolution of the established arc plasma, while microscopic non-equilibrium processes associated with arc inception, electrode sheaths, and the final extinction stage are outside the scope of the present model.

Under the local thermodynamic equilibrium (LTE) assumption adopted in this study, the electrical conductivity of the high-temperature air plasma is strongly dependent on its local thermodynamic state. Variations in temperature and pressure affect the equilibrium composition and concentration of charged species and therefore the electrical conductivity. Previous equilibrium-air-plasma studies have reported significant temperature- and pressure-dependent variations in electrical conductivity over broad thermodynamic ranges [21,22].

In the present model, two localized high-temperature seed channels with an initial temperature of 5000 K are prescribed across the armature–rail gap in ANSYS Fluent to establish the initial post-breakdown conductive state, as described above. The conductivity of these seed channels and the surrounding plasma region is not determined by a prescribed analytical breakdown criterion. Instead, the local electrical conductivity is obtained from tabulated thermophysical-property data through a user-defined function (UDF). The database covers temperatures from 300 to 30,000 K and pressure levels of 10,000, 100,000, and 1,000,000 Pa. During each Fluent solution step, the local temperature T and pressure p are used as interpolation variables to determine the corresponding electrical conductivity by linear interpolation, which can be expressed generally as:

$$\sigma = \sigma(T, p) \tag{1}$$

where σ denotes the local electrical conductivity, T is the local thermodynamic temperature, and p is the local pressure. After initialization, the conductivity field evolves dynamically with the temperature and pressure fields. The updated conductivity is transferred from ANSYS Fluent to ANSYS Maxwell through the System Coupling interface, while the electromagnetic solver provides the current density and Joule-heating source terms required by the Fluent calculation. Therefore, the initial 5000 K seed channels establish the conductive starting state, whereas the temperature- and pressure-dependent conductivity

data govern the subsequent nonlinear evolution of current redistribution, Joule heating, and arc development.

Radiative Energy Loss Treatment: Radiative energy loss from the high-temperature arc plasma is considered using a net-emission-coefficient (NEC)-based approach. The NEC is introduced as a thermophysical property of the plasma and obtained from tabulated data according to the local thermodynamic state. In ANSYS Fluent, a user-defined function (UDF) is employed to interpolate the NEC data and introduce the resulting radiative loss as a volumetric energy sink in the plasma energy equation. The radiative source term is expressed as

$$Srad = -4\pi NEC(T, p) \tag{2}$$

where S_{rad} denotes the volumetric radiative energy-loss term and NEC(T, p) is the net emission coefficient obtained from the tabulated data. This treatment accounts for the macroscopic radiative energy loss of the high-temperature plasma without explicitly resolving the full spectral radiative-transfer process.

2.3. Electromagnetic Field Model

To accurately capture the transient current conduction and electromagnetic field evolution during the rail launch, a three-dimensional electromagnetic model is established using the ANSYS Maxwell solver. Governed by the fundamental Maxwell's equations, the model calculates the spatial distributions of current density, electric field intensity, magnetic flux density, and volumetric Lorentz force across the rails, armature, and bypass arc chute. Furthermore, it achieves a rigorous two-way multiphysics coupling with ANSYS Fluent via the System Coupling platform.

Current continuity equation:

$$\nabla \cdot J = 0 \tag{3}$$

where J denotes the current density vector (A/m^2). This equation enforces the principle of charge conservation, thereby ensuring the continuous conduction of current throughout the entire conductive loop.

Faraday's Law of Electromagnetic Induction:

$$\nabla \times E = -\frac{\partial B}{\partial t} \tag{4}$$

where E and B represent the electric field intensity vector (V/m) and the magnetic flux density vector (T), respectively. This equation describes the transient coupling relationship between the time-varying magnetic field and the induced electric field.

Ampere's circuital law:

$$\nabla \times H = J \tag{5}$$

where H denotes the magnetic field intensity vector ("A/m"). This equation is utilized to calculate the spatial distribution of the magnetic field surrounding the rails, armature, and bypass arc chute, serving as a critical foundation for acquiring the volumetric Lorentz force.

Magnetic flux continuity equation:

$$\nabla \cdot B = 0 \tag{6}$$

This equation implies that the magnetic flux density consistently maintains a continuous spatial distribution, mathematically verifying the non-existence of magnetic monopoles. It serves as a fundamental constraint that must be rigorously satisfied during the electromagnetic field computation process.

Ohm's Law:

$$J = \sigma E \tag{7}$$

where σ represents the electrical conductivity of the materials (S/m).

For the solid computational domains, including the rails, armature, and bypass arc chute, the intrinsic electrical conductivities of the respective materials are adopted. Conversely, the electrical conductivity of the air domain is dynamically computed in real-time by ANSYS Fluent based on the localized temperature field and the transient developmental state of the plasma. These updated properties are subsequently fed back to ANSYS Maxwell to achieve the dynamic updating of the conductive characteristics during the air dielectric breakdown process.

Joule Heating:

$$Q = J \cdot E \tag{8}$$

where Q denotes the volumetric Joule heating density (W/m^3).

Serving as a critical energy source term transferred from the electromagnetic domain to the fluid flow field, the Joule heat is mapped into ANSYS Fluent to participate in the computation of the arc temperature field.

Lorentz Force:

$$F = J \times B \tag{9}$$

where F denotes the volumetric electromagnetic force vector (N/m^3).

The Lorentz force acts as the primary propulsive source driving the armature motion and serves as a critical benchmark for analyzing the asymmetric electromagnetic disturbances induced by the transient muzzle arc. In subsequent sections, the electromagnetic loading characteristics and transient overloads of the armature will be comprehensively evaluated in conjunction with the spatial distributions of the Lorentz force at various chronological tracking points.

2.4. Arc Plasma Flow Model

Following armature–rail separation, the transient arc plasma is modeled in ANSYS Fluent as a single-fluid compressible plasma under the local thermodynamic equilibrium (LTE) assumption. The fluid solver resolves the mass, momentum, and energy conservation equations. The electromagnetic quantities required by the plasma-flow calculation are obtained from ANSYS Maxwell. In particular, ANSYS Fluent updates the electrical conductivity of the arc plasma according to the local temperature through the UDF-based property treatment, and the updated conductivity is transferred to ANSYS Maxwell through the System Coupling interface. Maxwell then calculates the electric potential, current-density distribution, magnetic flux density, volumetric Lorentz-force density, and Joule-heating density. The Lorentz-force density and Joule-heating density are transferred back to Fluent as volumetric momentum and energy source terms.

Continuity equation:

$$\frac{\partial \rho}{\partial \mathrm{t}} + \nabla \cdot (\rho u) = 0 \tag{10}$$

where ρ denotes the fluid density (kg/m^3) and v represents the velocity vector (m/s).

Enforced by the law of conservation of mass, this equation governs the mass transport and the dynamic density evolution of the arc plasma within the high-speed flow domain.

Momentum equation:

$$\frac{\partial (\rho u)}{\partial t} + \nabla \cdot (\rho u u) = -\nabla p + \nabla \cdot \tau + F \tag{11}$$

where p denotes the static pressure (Pa), τ represents the viscous stress tensor (Pa), and F is the volumetric Lorentz force vector (N/m^3) computed by ANSYS Maxwell.

This governing equation describes the dynamic flow behavior and velocity field evolution of the arc plasma driven by the fluid-electromagnetic coupled forces.

Energy equation:

$$\frac{\partial(\rho h)}{\partial t} + \nabla \cdot (\rho u h) = \nabla \cdot (k \nabla T) + Q \quad (12)$$

where h denotes the specific enthalpy (J/kg), k represents the thermal conductivity ($W/(m \cdot K)$), and T is the thermodynamic temperature (K). Additionally, Q signifies the volumetric Joule heating source term (W/m^3) imported from ANSYS Maxwell.

This governing equation is primarily employed to resolve the transient spatial evolution profiles of the temperature field throughout the developmental phase of the muzzle arc.

2.5. Bidirectional Coupling Strategy

To establish the transient interaction between the electromagnetic field and the arc-plasma flow field, a bidirectional co-simulation framework between ANSYS Maxwell and ANSYS Fluent is established through the ANSYS System Coupling platform. Within each transient coupling step, ANSYS Maxwell uses the electrical conductivity distribution supplied by ANSYS Fluent to solve the electromagnetic conduction and field problem. Maxwell calculates the electric potential, current-density distribution, magnetic flux density, volumetric Lorentz-force density, and Joule-heating density in the electromagnetic domain.

The calculated volumetric Lorentz-force density and Joule-heating density are then transferred from ANSYS Maxwell to ANSYS Fluent as volumetric momentum and energy source terms. Fluent solves the mass, momentum, and energy conservation equations of the arc plasma and obtains the updated local temperature field. Based on the local thermodynamic state, the electrical conductivity of the arc plasma is updated through the UDF-based thermophysical-property treatment. The updated conductivity distribution is subsequently transferred from Fluent to Maxwell through the System Coupling interface for the next electromagnetic solution.

In the initial state, two localized high-temperature seed channels are prescribed across the armature–rail gap in ANSYS Fluent, with an initial temperature of 5000 K, to establish the initial conductive plasma state. The microscopic dielectric-breakdown inception process is not explicitly resolved in the present macroscopic model. During the subsequent transient calculation, the local plasma electrical conductivity is determined from the tabulated thermophysical-property data through the UDF-based linear interpolation procedure and updated according to the local thermodynamic state.

Through this bidirectional data-exchange mechanism, the coupled model captures the nonlinear transient evolution of the initially prescribed conductive arc, including changes in plasma temperature and electrical conductivity, current-density redistribution, Joule heating, plasma expansion, and electromagnetic-field distortion. The resulting electromagnetic quantities are continuously updated through the Maxwell–Fluent coupling procedure, thereby characterizing the transient evolution of the muzzle arc during the post-exit stage, as schematically illustrated in Figure 3.

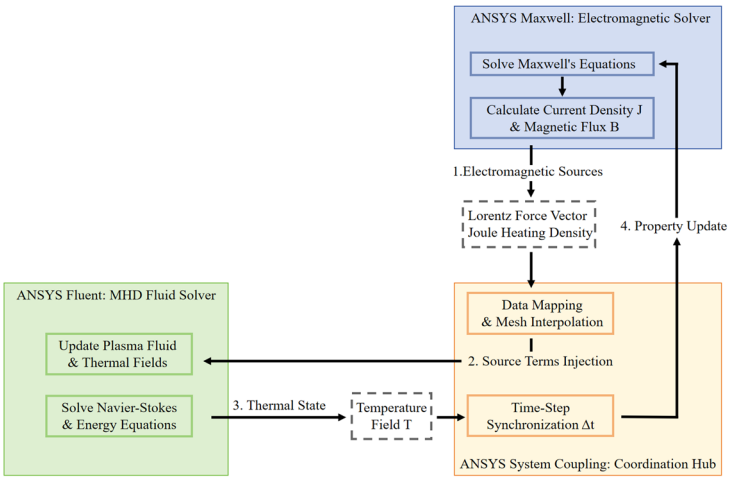


Figure 3. Schematic diagram of Fluent-Maxwell coupling based on System Coupling.

The armature dynamics are evaluated from the electromagnetic force obtained during the coupled field calculation. Specifically, the Lorentz-force density acting on the armature is integrated over its volume to obtain the resultant force components, which are then used to determine the translational acceleration response. In the present formulation, the armature is restricted to translational motion and its rotational degrees of freedom are not resolved. The resulting translational acceleration is therefore treated as a response quantity of the coupled electromagnetic–plasma fields rather than as an additional motion variable fed back into the Maxwell–Fluent field solution.

2.6. Boundary Conditions and Numerical Settings

To guarantee the numerical stability and computational accuracy of the bidirectional coupled simulations between the electromagnetic field and the plasma flow field, a unified configuration for the electromagnetic domain, fluid field, and numerical solution procedures is established in accordance with the evolutionary characteristics of the transient muzzle arc during the electromagnetic rail launch process. The primary boundary conditions and key numerical parameters are detailed below:

2.6.1. Electromagnetic Boundary Conditions

An 18 kA transient pulse current is applied at the rail breech end, with a zero-potential current return designated at the opposite end. External boundaries employ Magnetic Insulation to confine magnetic diffusion and enhance solver stability. The rails, armature, and bypass arc chute feature dynamic, temperature-dependent electrical conductivities that exchange data in real-time with the fluid solver via ANSYS System Coupling.

2.6.2. Fluid and Thermal Boundary Conditions

The far-field air boundaries are specified as Pressure Outlet (101,325 Pa, 300 K), while solid surfaces utilize No-slip Wall conditions. Furthermore, Thermal Continuity is enforced at all fluid-solid interfaces to permit the bidirectional transport of conduction, convection, and Joule heating, rigorously ensuring multiphysics energy conservation.

2.6.3. Transient Coupling Solver Settings

A bidirectional transient co-simulation is established between ANSYS Maxwell (electromagnetic sources) and ANSYS Fluent (plasma dynamics), with data mapped via System Coupling. To capture the rapid variations during arc propagation, a fixed time step of 1 μs is selected. Within each step, data exchange and inner iterations are performed until convergence before advancing to the next step, ensuring strict temporal synchronization.

2.6.4. Mesh Generation and Numerical Settings

The computational domain is discretized using an unstructured tetrahedral mesh. For the surface mesh, the minimum and maximum element sizes are set to 0.1 and 2 mm, respectively. Curvature- and proximity-based size functions are employed, with a curvature normal angle of 18° and three cells per gap. The volume mesh is generated using Fluent with a global sizing strategy, a growth rate of 1.19999, and a maximum cell length of 2.551 mm. Both fluid and solid regions are included in the meshing process. Local mesh refinement is applied around the muzzle exit, armature trailing edge, and arc region to better resolve the strong spatial gradients in these critical regions.

The resulting computational mesh contains 187,611 cells. The minimum cell quality is 0.3146, and no cells have a quality below 0.05, indicating that the mesh contains no severely distorted elements. A double-precision solver with second-order discretization schemes is subsequently employed for the multiphysics calculations.

A fixed time step of 1 μs is adopted for the transient multiphysics calculations throughout the simulated time interval. The same coupling interval is used for the electromagnetic, thermal, and plasma-flow field updates to ensure consistent temporal synchronization between ANSYS Maxwell and ANSYS Fluent.

3. Transient Arc Evolution Mechanism During Armature-Rail Separation

3.1. Arc Formation and Current Density Evolution

Upon the armature's exit, the abrupt rupture of the solid electrical contact triggers a sharp impedance surge due to the residual circuit energy. Immediately after armature–rail separation, two localized high-temperature seed channels bridge the transient gap between the rail leading edges and the armature tail. These channels provide the initial conductive paths for the post-breakdown plasma. As the simulation proceeds, Joule heating modifies the local temperature field, while the temperature-dependent electrical conductivity changes the current-density distribution. The updated conductivity is continuously transferred from Fluent to Maxwell through the System Coupling framework, thereby governing the subsequent evolution of the arc current density, temperature field, plasma flow, and electromagnetic field. Figure 4 illustrates the 3D spatial evolution of the arc current density at various post-exit instants in the absence of a bypass arc chute.

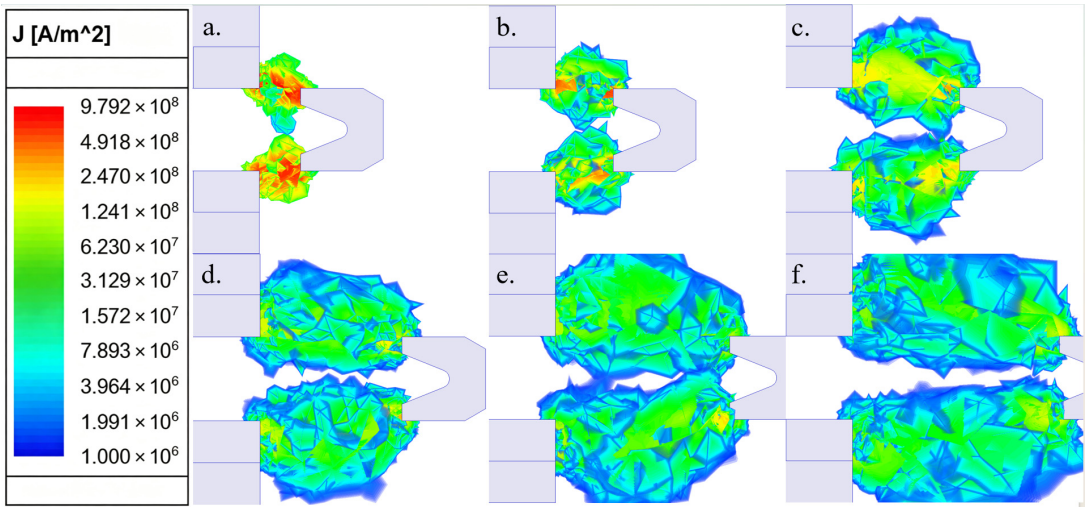


Figure 4. Contour cloud of arc current density between armature and rails without arc chute. (**a**–**f**) represent six successive post-exit time instants.

The transient arc evolution undergoes three distinct stages: initial extreme concentration, violent expansion, and highly non-uniform energy retention. Immediately upon exit, a narrow plasma channel forms, surging the peak current density to 9.792×10^8 A/m^2 and initiating pronounced localized Joule heating. As the armature advances, thermal expansion and Lorentz forces drive the arc to violently expand from a localized spot into a dispersed three-dimensional cloud, corresponding to the process from (a) to (f) in Figure 4. Finally, although spatial expansion dilutes the current density, In the absence of a bypass path, the imposed current continues to be conducted through the evolving plasma channel, while the increasing arc length, spatial expansion, and temperature-dependent conductivity govern the redistribution of current density.

The transient muzzle-arc evolution obtained in the present study is qualitatively consistent with previous numerical and experimental investigations of electromagnetic railgun muzzle arcs. Zhao et al. [13] employed a three-dimensional multiphysics model to analyze the transient muzzle-arc flow field and reported strong temporal evolution of the arc and its associated electromagnetic characteristics. Gao et al. [23] further combined magnetohydrodynamic simulation with railgun prototype experiments and compared the simulated muzzle voltage with experimental measurements, providing an external reference for the transient arc evolution. More recently, high-speed imaging experiments have been used to directly characterize the temporal evolution and spatial motion of electromagnetic railgun muzzle arcs [24]. These previous studies provide a literature-based consistency reference for the transient arc evolution predicted in the present work.

3.2. Temperature Field Evolution and Thermal Loading Characteristics

Building upon the preceding current density analysis, the extreme localized current density within the plasma channel consequently induces intense volumetric Joule heating. Consequently, Figure 5 illustrates the three-dimensional dynamic evolution of the transient arc temperature field between the armature and rails at various post-exit instants, in the absence of a bypass arc chute.

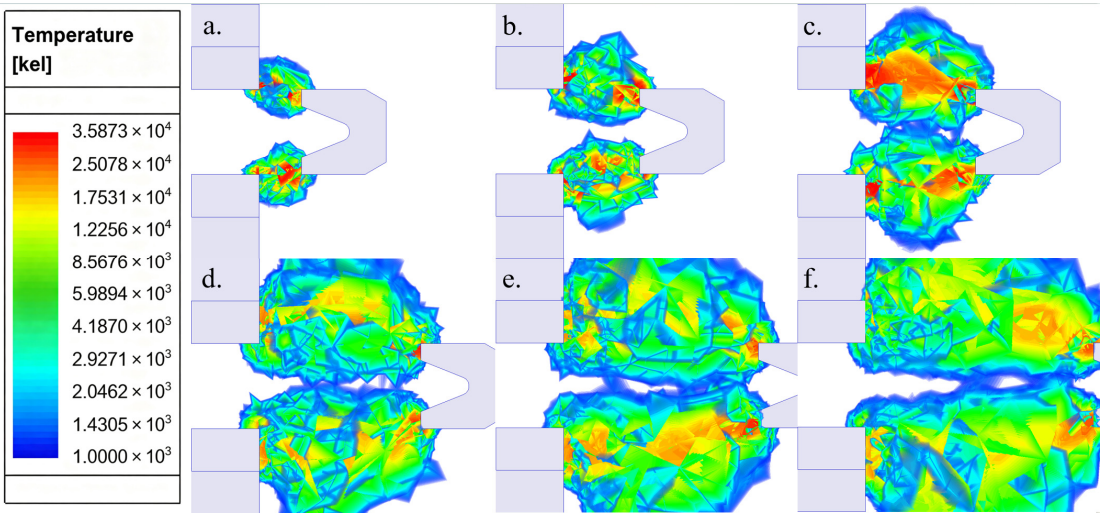


Figure 5. Contour plot of arc temperature between armature and rails without an arc chute. (**a**–**f**) represent six successive post-exit time instants.

Driven primarily by Joule heating, the arc temperature and current density fields exhibit strong spatio-temporal coupling that governs the thermal response of the muzzle region. Immediately post-exit, immense volumetric Joule heating within the narrow discharge channel generates an extreme thermal core, with the peak plasma temperature surging to 35,873 K. As the plasma subsequently expands, convection partially dilutes the thermal

load; however, lacking an external low-impedance bypass, causing the high-temperature plasma cloud to persistently stagnate between the armature tail and the muzzle.

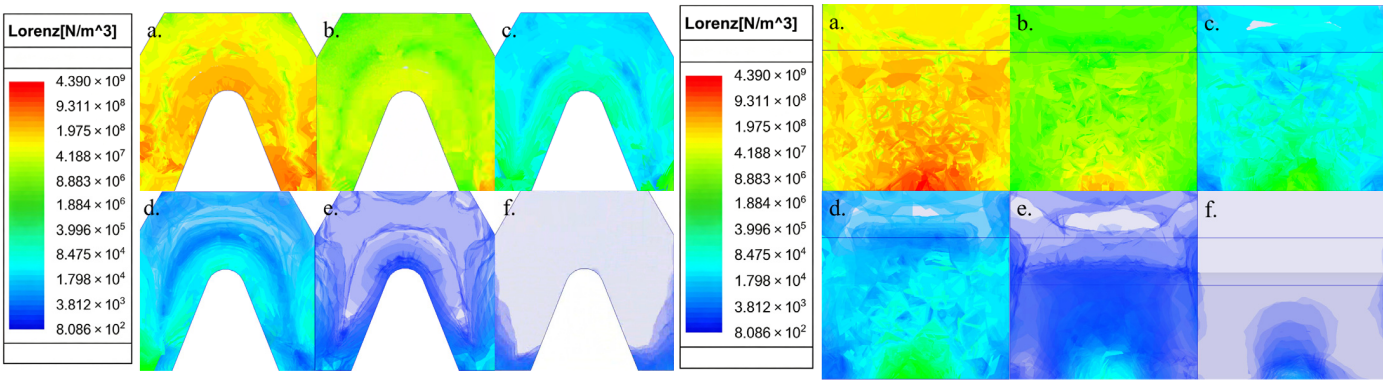
Multiphysics Thermal and Electromagnetic Effects: This intense thermal loading produces strong thermal exposure in the muzzle region, particularly near the rail ends and armature tail. The predicted temperature field indicates a strong thermal environment that may contribute to localized thermally induced material degradation. However, quantitative material melting, vaporization, surface recession, or mass-loss processes are not explicitly resolved in the present model. Therefore, the present results are interpreted in terms of thermal loading and potential material degradation rather than direct predictions of ablation or asymmetric mass loss. The associated thermal and electromagnetic fields are then considered in evaluating the transient dynamic disturbance of the armature after rail separation.

3.3. Resultant Lorentz Force and Electromagnetic Loading

Upon exiting the rigid rail constraints, the conductive medium transitions from solid metal to freely expanding plasma. The highly non-uniform and asymmetric spatial diffusion of this plasma induces severe topological distortion in the current density vector J. Consequently, this distorted conduction source excites an asymmetric magnetic field B, thereby mapping an extremely unbalanced Lorentz force field onto the armature surface via $F = J \times B$.

3.3.1. Spatial Concentration and Evolution of Volumetric Lorentz Force Density

A To quantitatively evaluate the transient impact of the distorted electromagnetic fields on the armature, the spatial magnitude distributions of the volumetric Lorentz force at various post-exit stages were extracted. As depicted in the side and top contour plots of the armature in Figure 6:



(**A**) (**B**)

Figure 6. Lorentz force contours of armature at various stages after muzzle exit. (**A**) Side view, snapshots (**a**–**f**) represent successive time moments; (**B**) Top view, snapshots (**a**–**f**) represent the corresponding successive time moments.

Immediately post-exit, the peak local volumetric Lorentz-force density reaches 4.39×10^9 N/m^3, concentrating asymmetrically at the armature's inner U-shaped groove and trailing edges in close correspondence with the arc attachment regions. Although the peak force gradually decreases as the plasma expands, the force field maintains a distinctly non-uniform spatial distribution throughout the post-exit interval, indicating persistent asymmetry in the electromagnetic loading acting on the armature.

3.3.2. Directional Imbalance of Force Field and Attitude Perturbation Torque

While the magnitude contours identify the regions of concentrated electromagnetic loading, the directional distribution of the Lorentz-force vectors further characterizes the three-dimensional loading state acting on the armature. To quantify the net electromagnetic loading after rail separation, the volumetric Lorentz-force density is integrated over the armature volume:

$$F_L(t) = \int_{Va} f_L(r,t)dV = [F_x(t), F_y(t), F_z(t)] \quad (13)$$

where V_a denotes the armature volume and $\boldsymbol{f}_L$ is the local volumetric Lorentz-force density. The resulting components F_x, F_y, and F_z represent the net electromagnetic loading acting on the armature along the three coordinate directions. As illustrated in Figure 7, the Lorentz-force vectors exhibit pronounced spatial non-uniformity after rail separation, indicating asymmetric electromagnetic loading in the transverse and normal directions.

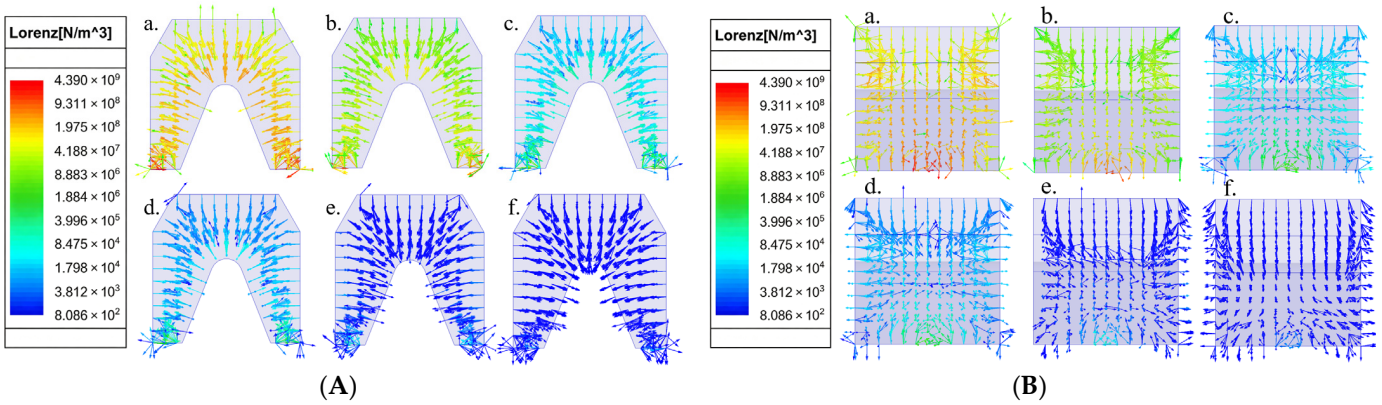


Figure 7. Vector plots of Lorentz force distribution on the armature at different instants after muzzle exit. (**A**) Side view, internal sub-panels (**a**–**f**) correspond to successive time instants; (**B**) Top view, internal sub-panels (**a**–**f**) represent the corresponding successive time instants.

For the translational armature model adopted in this study, the corresponding acceleration is obtained from Newton's second law:

$$\mathrm{a}(t) = \frac{F_L(t)}{\mathrm{m_a}} \quad (14)$$

where m_a is the armature mass.

The vector plots reveal pronounced three-dimensional directional imbalances in the electromagnetic loading. In the Z direction, the non-uniform force distribution produces significant normal loading fluctuations, while the asymmetric X-direction force distribution generates a net transverse electromagnetic disturbance. These force components act on the armature after the loss of rail constraint and are reflected in the corresponding off-axis translational acceleration response discussed in Section 3.4.

Combining the results in Figures 6 and 7, the spatially dispersed muzzle arc produces strongly non-uniform electromagnetic loading on the armature, particularly near the tail and inner groove regions. The resulting directional imbalance in the Lorentz-force distribution provides the electromagnetic origin of the lateral and normal translational acceleration disturbances observed after rail separation.

3.4. Three-Dimensional Transient Dynamic Response of the Armature

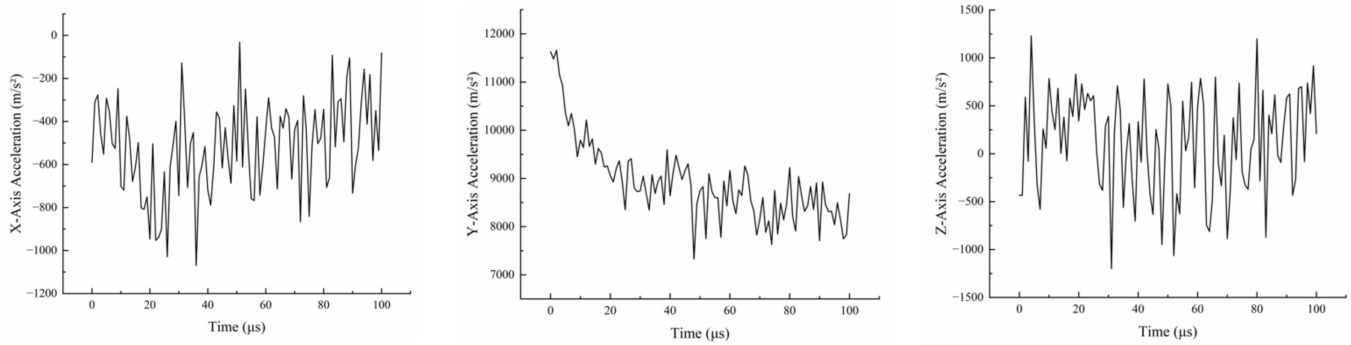
Following armature–rail separation, the electromagnetic loading obtained from the coupled field calculation acts on the armature as a transient external force. In the present model, the armature is treated as a translationally moving body, and its rotational degrees

of freedom are not considered. The resultant Lorentz-force components are therefore used to evaluate the corresponding translational accelerations along the three orthogonal axes.

To evaluate the influence of the transient muzzle arc on the post-exit dynamic response of the armature, the acceleration components along the three orthogonal directions are analyzed. The axial acceleration represents the dominant longitudinal response, whereas the X- and Z-direction components characterize the off-axis translational disturbances associated with the asymmetric Lorentz-force distribution.

The time-varying curves demonstrate that while axial (Y-axis) acceleration dominates, transverse (X-axis) and normal (Z-axis) accelerations manifest primarily as pronounced transient perturbations.

As depicted in Figure 8, the transient accelerations across the three orthogonal axes exhibit distinct dynamic responses. The axial (Y-axis) acceleration dominates the post-exit kinematics, rapidly peaking at 11,660.25 m/s^2 (approx. 1188.6 g) at 2 μs due to residual current thrust, before slowly decaying as arc impedance increases. Conversely, the transverse (X-axis) acceleration remains consistently negative, peaking at −1069.92 m/s^2 (approx. 109.1 g) at 36 μs. This is driven by early asymmetric Lorentz forces at the armature tail, inducing strong lateral impact. Simultaneously, the normal (Z-axis) acceleration exhibits a pronounced positive-negative oscillation—ranging from 1228.94 m/s^2 to 1199.18 m/s^2, reflecting continuous spatial offsets of the normal electromagnetic force that directly generate transient pitching moments.



(**a**) (**b**) (**c**)

Figure 8. Time-varying curves of armature accelerations in different directions without arc chute. (**a**) X-axis acceleration (transverse); (**b**) Y-axis acceleration (axial); (**c**) Z-axis acceleration (normal).

In summary, the spatially asymmetric Lorentz forces induced by the muzzle arc dictate these multi-directional transient overloads. While the dominant Y-axis acceleration governs the armature's residual propulsion, the intense, albeit brief, transverse (109.1 g) and normal (125.3 g) overloads significantly elevate the risks of yaw and pitch instability. Consequently, mitigating the transient arc intensity and suppressing these asymmetric electromagnetic loads are imperative for enhancing the armature's exterior ballistic stability and overall launch precision.

4. Mechanism and Performance Evaluation of Arc Chute

4.1. Regulating Effect of the Arc Chute on the Current Path

Figure 9 illustrates the transient evolution of arc current density post-exit with the bypass arc chute. By altering the residual current path, the chute gradually redirects the current from the main circuit to the bypass branch, thereby effectively suppressing muzzle arc development.

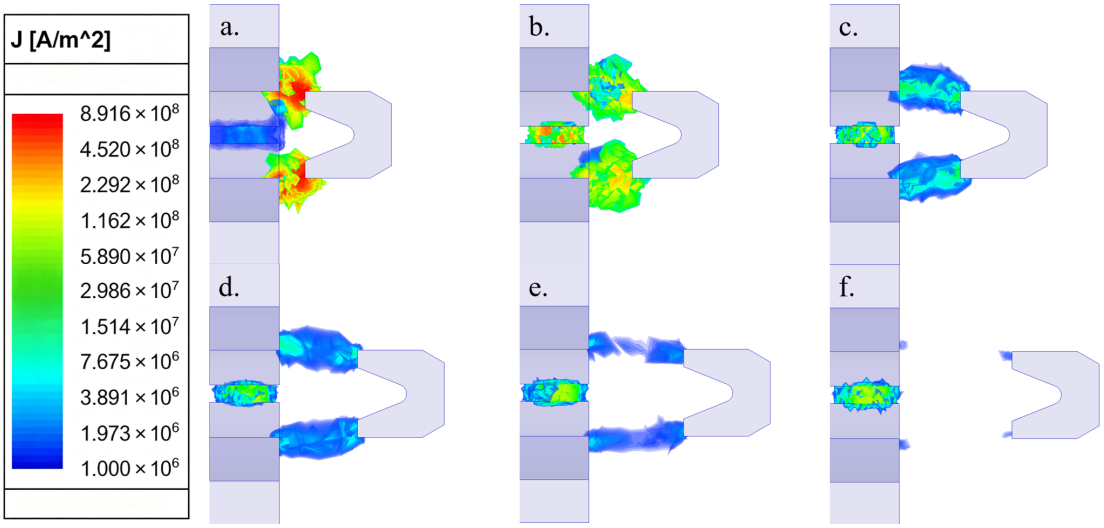


Figure 9. Contour plots of arc current density at various post-exit stages with the bypass arc chute. (**a**–**f**) represent six successive post-exit time instants.

At the initial stage after muzzle exit, the main circuit remains conductive, and high current density of 8.916×10^8 A/m^2 concentrates at the arc roots between the rails and the armature tail. As the armature travels forward, the elongated main arc brings about increased equivalent impedance and rising muzzle voltage, which eventually triggers dielectric breakdown at the gap of the arc chute, corresponding to the process from (a) to (c) in Figure 9. A new plasma channel is thereby formed, enabling rapid redistribution of residual current toward the bypass branch. At this moment, the bypass current density rises sharply, while the main armature-rail arc gradually decays and extinguishes, corresponding to the process from (d) to (f) in Figure 9. By approximately 44 μs, the main armature–rail arc is substantially suppressed in the arc-chute configuration, whereas the main arc remains present throughout the reported 120 μs simulation interval in the absence of the arc chute. Because the present calculation does not extend beyond 120 μs, no extrapolation of the arc lifetime beyond the simulated interval is made.

Compared with the configuration without an arc chute, the current-density evolution demonstrates a clear redistribution of the imposed current after armature–rail separation. Without the arc chute, the current density remains concentrated within the main armature–rail arc and persists in the muzzle region, indicating that the current continues to be conducted through the elongated arc path. With the arc chute, the current density progressively shifts toward the bypass branch, while the current-density concentration within the main armature–rail arc decreases as the discharge develops. This contrast indicates that the primary effect of the arc chute is to regulate the spatial current path rather than to change the prescribed total excitation current of 18 kA.

In summary, the bypass arc chute regulates the spatial distribution of the imposed current by providing a low-impedance bypass path. The current-density results show that the main armature–rail arc progressively loses its dominant conduction role after the bypass branch is established. This current-path redistribution reduces the duration and spatial concentration of the main arc, thereby reducing the associated Joule-heating concentration in the muzzle region. The resulting changes in the temperature field and electromagnetic loading are discussed in Sections 4.2 and 4.3, respectively.

4.2. Suppression of Thermal Loading by the Arc Chute

Figure 10 illustrates the transient evolution of the muzzle arc temperature field with the bypass arc chute. Compared to the condition without an arc chute, the establishment of

the bypass discharge channel forces the arc heat source to migrate from the inter-rail gap to the chute zone. This migration significantly shrinks the high-temperature region within the main circuit, thereby effectively mitigating the strong thermal loads exerted on the rail ends and the armature tail.

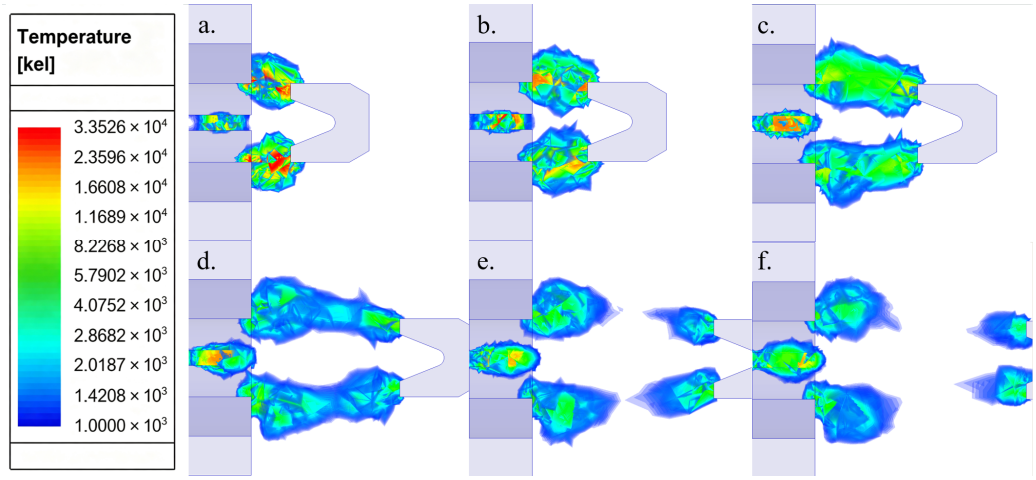


Figure 10. Contour plots of temperature at various post-exit stages with the bypass arc chute. (**a**–**f**) represent six successive post-exit time instants.

Initially upon exit, the main circuit remains conductive, rapidly forming an armature-rail arc with a high-temperature plasma core concentrated between the armature tail and the rail ends; its peak temperature drops slightly to 33,526 K compared with the condition without an arc chute. Concurrently, localized discharge channels initiate at the arc chute, sparking a new high-temperature zone that signifies the onset of current shunting to the bypass branch. As the armature-rail arc subsequently elongates, its increasing equivalent resistance forces more residual current through the chute. This shift rapidly suppresses the armature-rail Joule heating, causing the high-temperature core at the rail ends to shrink substantially while the thermal zone near the arc chute intensifies, indicating a definitive migration of the primary heat source to the bypass circuit.

During the late discharge stage, the main circuit arc is virtually extinguished, and the armature-rail high-temperature zone vanishes completely, leaving only a localized plasma cloud at the arc chute. Crucially, as the discharge site moves away from the muzzle, the rail ends and the armature tail are shielded from continuous high-temperature thermal loading. Ultimately, the bypass arc chute does not simply reduce the peak temperature, but rather alters the residual current path to actively relocate the thermal core. This mechanism curtails the main arc duration, isolates key muzzle structures from intense thermal environment, and lays a vital physical foundation for mitigating subsequent electromagnetic perturbations and stabilizing the armature's post-exit flight attitude.

4.3. Suppression of Electromagnetic Perturbations by the Arc Chute

A To further evaluate the efficacy of the bypass arc chute in enhancing post-exit stability, the transient accelerations along the *X*-, *Y*-, and *Z*-axes with and without the arc chute are compared in Figure 11. Overall, implementing the arc chute markedly suppresses the transverse and normal transient overloads while curtailing the duration of electromagnetic perturbations, yielding a much smoother dynamic response. The mitigation of these disturbances is most pronounced along the *X*- and *Z*-axes, whereas the axial (*Y*-axis) propulsion is marginally affected.

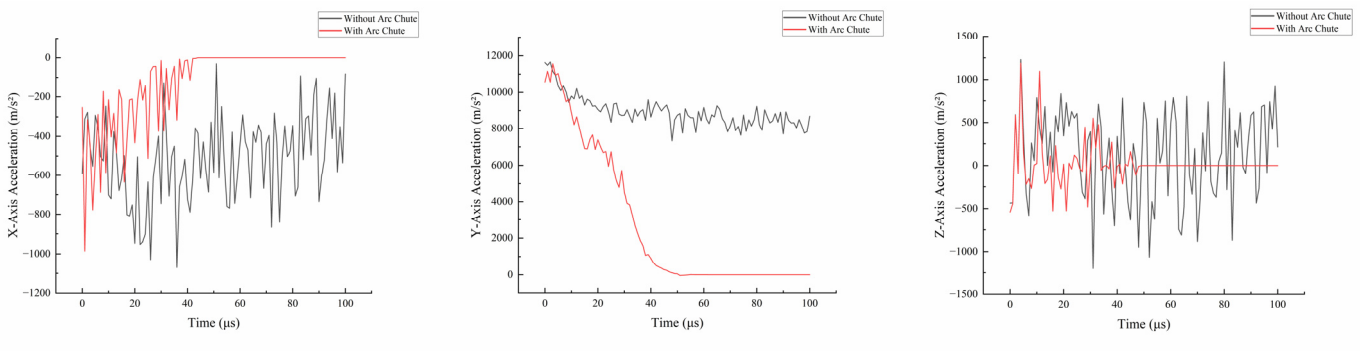


Figure 11. Comparison of the armature's transient accelerations along different axes over time with and without the bypass arc chute. (**a**) X-axis acceleration (transverse); (**b**) Y-axis acceleration (axial); (**c**) Z-axis acceleration (normal).

As shown in Figure 11a,b, in the absence of the arc chute, the X-axis acceleration exhibits strong negative oscillations peaking near -1000 m/s^2 throughout the discharge, indicating a persistent transverse asymmetric Lorentz force. Conversely, the arc chute rapidly dampens these fluctuations via current shunting, causing them to decay to zero by 50 μs and significantly mitigating yaw risks. Axially (Y-axis), the unchuted armature experiences sustained propulsion (8000 to 11000 m/s^2) from the residual arc. With the arc chute, the Y-axis acceleration drops to zero by 50 μs as the current shifts to the bypass. Notably, this rapid axial decay reflects accelerated residual energy dissipation rather than degraded propulsion efficiency, successfully preventing prolonged, destructive arc interactions at the muzzle. Regarding the normal (Z-axis) dynamics in Figure 11c, this condition exhibits intense positive-negative oscillations exceeding ± 1200 m/s^2, underscoring highly fluctuating normal electromagnetic loads that induce strong pitching vibrations. Implementing the bypass arc chute effectively suppresses these Z-axis oscillations, which stabilize after approximately 50 μs. This rapid stabilization demonstrates that the arc chute successfully attenuates the normal asymmetric Lorentz force and its associated transient torque, thereby substantially enhancing the armature's pitching stability.

In summary, the multi-directional dynamic responses confirm that the bypass arc chute drastically curtails the duration of electromagnetic perturbations. The marked dampening of X- and Z-axis oscillations verifies the effective suppression of asymmetric lateral and normal loads, while the rapid decay of Y-axis acceleration ensures the prompt discharge of residual electromagnetic energy. Ultimately, through the integrated mechanism of current shunting, heat source migration, and electromagnetic perturbation mitigation, the bypass arc chute minimizes post-exit yaw and pitch instability risks, contributing to flight attitude stability and overall launch precision.

The above comparison with previous studies should be interpreted as a qualitative consistency assessment rather than direct quantitative validation of the present model. Because the cited studies involve different launcher configurations, operating conditions, and measurement quantities, direct quantitative validation of the present temperature, electromagnetic loading, and armature acceleration results would require dedicated experiments or an independent numerical benchmark under matched conditions.

5. Conclusions

Aiming at the detrimental muzzle arc phenomenon during the armature-rail separation phase in electromagnetic rail launches, a two-way strongly coupled magnetohydrodynamic (MHD) numerical model integrating Ansys Maxwell and Fluent was established via the System Coupling platform. Utilizing a 10 mm $\times$ 10 mm scaled caliber device and

a 1.9 g aluminum alloy U-shaped armature as the research subjects, this study systematically elucidated the evolutionary mechanism of the muzzle discharge plasma and off-axis translational dynamic disturbances induced by transient electromagnetic loading. Furthermore, the comprehensive suppression efficacy of the bypass arc chute was quantitatively evaluated. The main conclusions are as follows:

A two-way strongly coupled electromagnetic-fluid-thermal numerical model was established. By dynamically updating the conductivity matrix and coupled source terms, it accurately reproduces the full-lifecycle evolution of the muzzle arc, effectively quantifying the complex interactions between spatial force field distortions and macroscopic dynamic responses.

Without the arc chute, the unconfined muzzle arc (peaking at 35,873 K) exhibits dual kinematic effects. While providing a sustained axial propulsion (11,000 − 12,000 m/s^2), its highly non-uniform and asymmetric expansion induces strong spatial Lorentz force imbalances. The asymmetric expansion of the unconfined muzzle arc produces significant multidirectional Lorentz-force imbalance and pronounced off-axis translational acceleration disturbances after rail separation.

The bypass arc chute effectively mitigates thermal and dynamic disturbances by redirecting residual current through a low-impedance channel. It actively relocates the extreme thermal core, curtails the main arc duration to 44 μs, and completely eliminates transverse and normal transient overloads within 50 μs. The bypass arc chute reduces the multidirectional electromagnetic acceleration disturbances and shortens the duration of the main arc, thereby mitigating the post-exit translational dynamic disturbance of the armature.

Author Contributions: Conceptualization, Project administration, Methodology, writing—review and editing, and funding acquisition, J.L.; Software, Validation, Formal analysis, Investigation, Visualization, and writing—original draft preparation, J.Y.; Data curation and Validation, X.T.; Data curation, C.C.; Data curation, Q.L.; Supervision, Y.F. All authors have read and agreed to the published version of the manuscript.

Funding: This research was funded by the National Natural Science Foundation of China (NSFC), grant number [92166204]. The APC was funded by the Jianyong Lou Research Group, School of Electrical Engineering, Xi'an Jiaotong University.

Data Availability Statement: The raw data supporting the conclusions of this article will be made available by the authors on request.

Conflicts of Interest: Author Yigong Feng was employed by the company State Grid Henan Electric Power Company Construction Branch. The remaining authors declare that the research was conducted in the absence of any commercial or financial relationships that could be construed as a potential conflict of interest.

References

1. Yang, Y.; Dai, K.; Yin, Q.; Liu, P.; Yu, D.; Li, H.; Zhang, H. In-Bore Dynamic Measurement and Mechanism Analysis of Multi-Physics Environment for Electromagnetic Railguns. *IEEE Access* **2021**, *9*, 16999–17010. [CrossRef]
2. Guo, Z.; Yuan, Z.; Jin, Y.; Chen, J.; Li, T. A Multi-Physics Field Modeling Approach for the Electromagnetic Railgun Launch of Intelligent Projectiles. *IEEE Access* **2024**, *12*, 134091–134100. [CrossRef]
3. Rodger, D.; Leonard, P.J. Modelling the Electromagnetic Performance of Moving Rail Gun Launchers Using Finite Elements. *IEEE Trans. Magn.* **1993**, *29*, 496–498. [CrossRef]
4. Ge, X.; Cao, B.; Wang, Z.; Pei, P.; Su, Z.; Chen, Y.; Guo, W.; Li, J. Analysis and Research on Muzzle Arc Suppression Device of Arc Striking Railgun. *IEEE Trans. Plasma Sci.* **2022**, *50*, 1337–1344. [CrossRef]
5. He, Y.; Cheng, C.; Song, S.; Guan, Y.; Gao, G.; Li, Y.; Qiu, X. Suppressing of Muzzle Arc during Railgun Launch. *High Power Laser Part. Beams* **2016**, *28*, 025003. [CrossRef]

6. Chen, L.; Xu, X.; Wang, Z.; Xu, J.; You, P.; Lan, X. Melting Distribution of Armature in Electromagnetic Rail Launcher. *IEEE Trans. Plasma Sci.* **2023**, *51*, 234–242. [CrossRef]
7. Wang, G.; Tian, W.; Zhao, W.; Zhao, Y.; Yuan, W.; Yan, P. Modeling the Temperature Evolution of Electromagnetic Rails under Multiphysics Coupling. *Case Stud. Therm. Eng.* **2025**, *75*, 107177. [CrossRef]
8. Ge, X.; Cao, B.; Wang, Z.; Pei, P.; Huang, K.; Chen, Y.; Fan, W.; Zhang, T. Research on the Contact Characteristics Between Armature and Rail of the Enhanced Electromagnetic Rail Gun Based on the New Aluminum Alloy Armature. *IEEE Trans. Plasma Sci.* **2023**, *51*, 3703–3708. [CrossRef]
9. Gleizes, A.; Gonzalez, J.J.; Freton, P. Thermal Plasma Modelling. *J. Phys. D Appl. Phys.* **2005**, *38*, R153–R183. [CrossRef]
10. Ren, S.; Feng, G.; Liu, S. Study on Wear of Electromagnetic Railgun. *IEEE Access* **2022**, *10*, 100955–100963. [CrossRef]
11. Santos, D.F.N.; Almeida, N.A.; Benilova, L.G.; Benilov, M.S. Model of Non-Equilibrium Near-Cathode Plasma Layers for Simulation of Ignition of High-Pressure Arcs on Cold Refractory Cathodes. *J. Phys. D Appl. Phys.* **2024**, *57*, 405202. [CrossRef]
12. Thanua, N.; Kumbhar, G.B. Numerical Methods for Multiphysics Modeling of Plasma Due to Electrical Discharge. *IEEE Trans. Plasma Sci.* **2024**, *52*, 1539–1545. [CrossRef]
13. Zhao, W.; Tian, W.; Yuan, W.; Yan, P. Muzzle Arc Flow Field Simulation of a Small Caliber Launcher. *IEEE Trans. Plasma Sci.* **2022**, *50*, 510–516. [CrossRef]
14. Zhao, Y.; Li, J.; Li, Y.; Ku, Z.; Dong, H. 10 Multiphysics Coupling Mechanism of Copper Vapor Diffusion–Extinction Vacuum Arc Plasma: Experiments, Simulations, and Theoretical Analysis. *IEEE Trans. Plasma Sci.* **2025**, *53*, 3053–3066. [CrossRef]
15. Kwon, Y.; Pratikakis, N.; Shellock, M.R. Multiphysics Modeling of a Rail Gun Launcher. *Int. J. Multiphysics* **2008**, *2*, 421–436. [CrossRef]
16. Yang, Y.; Dai, K.; Yin, Q.; Li, C.; Li, H.; Zhang, H. Multiphysics Coupling Simulation of Electromagnetic Railgun Based on the Field-Circuit Coupled Method. *J. Magn. Magn. Mater.* **2024**, *607*, 172403. [CrossRef]
17. Praneeth, S.R.N.; Singh, B. Investigations on Armature Jerk for Different Current Pulse and Rail Geometries in an Electromagnetic Railgun. *IEEE Trans. Plasma Sci.* **2024**, *52*, 1486–1491. [CrossRef]
18. Mao, W.; Pang, T.; Guo, Z.; Bai, H.; Huang, Z.; Jin, X. Analysis of the Research Progress of Electromagnetic Railgun Based on CiteSpace. *IEEE Access* **2024**, *12*, 3499–3513. [CrossRef]
19. Sun, J.; Cheng, J.; Wang, Q.; Xiong, L.; Cong, Y.; Wang, Y. Research on Arc Suppression Parameter Matching of Augmented Electromagnetic Launcher. *IEEE Trans. Plasma Sci.* **2021**, *49*, 3988–3993. [CrossRef]
20. Gu, B.; Li, H.; Li, B. An Internal Ballistic Model of Electromagnetic Railgun Based on PFN Coupled with Multi-Physical Field and Experimental Validation. *Def. Technol.* **2024**, *32*, 254–261. [CrossRef]
21. D'Angola, A.; Colonna, G.; Gorse, C.; Capitelli, M. Thermodynamic and transport properties in equilibrium air plasmas in a wide pressure and temperature range. *Eur. Phys. J. D* **2008**, *46*, 129–150. [CrossRef]
22. Raizer, Y.P. *Gas Discharge Physics*; Springer: Berlin, Germany, 1991.
23. Gao, Y.; Ni, Y.-J.; Wang, Z.-X.; Xu, Y.-T.; Jin, Y.; Li, B.-M. Modeling and simulation of muzzle flow field of railgun with metal vapor and arc. *Def. Technol.* **2020**, *16*, 802–810. [CrossRef]
24. Feng, J.; Liu, L.; Chen, X.; Zhang, L.; Cong, H.; Liu, H. Image processing method and morphological feature analysis of muzzle arc in electromagnetic railguns. *AIP Adv.* **2026**, *16*, 045314. [CrossRef]

Disclaimer/Publisher's Note: The statements, opinions and data contained in all publications are solely those of the individual author(s) and contributor(s) and not of MDPI and/or the editor(s). MDPI and/or the editor(s) disclaim responsibility for any injury to people or property resulting from any ideas, methods, instructions or products referred to in the content.